



Al-Afeef, A., Bobynko, J., Cockshott, W. P., Craven, A. J., Zuazo, I., Barges, P., and MacLaren, I. (2016) Linear chemically sensitive electron tomography using DualEELS and dictionary-based compressed sensing. Ultramicroscopy.

There may be differences between this version and the published version. You are advised to consult the publisher's version if you wish to cite from it.

<http://eprints.gla.ac.uk/122396/>

Deposited on: 22 August 2016

Enlighten – Research publications by members of the University of Glasgow
<http://eprints.gla.ac.uk>

Linear chemically sensitive electron tomography using DualEELS and dictionary-based compressed sensing

Ala AlAfeef^{a, b}, Joanna Bobynko^a, W. P. Cockshott^b, Alan J. Craven^a, Ian Zuazo^c, Patrick Barges^c, Ian MacLaren^{a, *}

^a*SUPA School of Physics and Astronomy, University of Glasgow, Glasgow G12 8QQ, UK*

^b*School of Computing Science, University of Glasgow, Glasgow G12 8QQ, UK*

^c*ArcelorMittal Maizières Research, Maizières-lès-Metz 57283, France*

ARTICLE INFO

ABSTRACT

Keywords:

DualEELS tomography
Vanadium carbide precipitates
High manganese steel
Electron tomography
Deconvoluted EELS data
Compressed sensing

We have investigated the use of DualEELS in elementally sensitive tilt series tomography in the scanning transmission electron microscope. A procedure is implemented using deconvolution to remove the effects of multiple scattering, followed by normalisation by the zero loss peak intensity. This is performed to produce a signal that is linearly dependent on the projected density of the element in each pixel. This method is compared with one that does not include deconvolution (although normalisation by the zero loss peak intensity is still performed). Additionally, we compare the 3D reconstruction using a new compressed sensing algorithm, DLET, with the well-established SIRT algorithm. VC precipitates, which are extracted from a steel on a carbon replica, are used in this study. It is found that the use of this linear signal results in a very even density throughout the precipitates. However, when deconvolution is omitted, a slight density reduction is observed in the cores of the precipitates (a so-called cupping artefact). Additionally, it is clearly demonstrated that the 3D morphology is much better reproduced using the DLET algorithm, with very little elongation in the missing wedge direction. It is therefore concluded that reliable elementally sensitive tilt tomography using EELS requires the appropriate use of DualEELS together with a suitable reconstruction algorithm, such as the compressed sensing based reconstruction algorithm used here, to make the best use of the limited data volume and signal to noise inherent in core-loss EELS.

1. Introduction

Electron tomography (ET) is now increasingly important for recovering the three-dimensional (3D) morphology of nanostructured materials in the physical and life sciences [1,2]. ET typically involves the acquisition of a set of two-dimensional projection images at different tilts using (scanning) transmission electron microscopy ([S]TEM), followed by alignment and reconstruction using established algorithms to reconstruct a 3D volume that represents the physical morphology or 3D distribution or other property of the specimen under investigation. In principle, the methodology is independent of the nature of the images and is applicable to any imaging technique that fulfils the projection requirement [3] such that the signal should change monotonically with the physical property of the sample. This condition is approximately fulfilled for mass-thickness contrast in bright field TEM of amorphous biological specimens, and, to a lesser extent, high angle annular dark field (HAADF) STEM imaging of thin specimens. Consequently, both imaging techniques have been widely used in ET.

Recently, ET has been performed using spectroscopic signals, including X-ray spectroscopy [51,52], energy-filtered TEM (EFTEM) [53–56], and electron energy loss spectroscopy (EELS) [6,7,57] in

the STEM, to achieve a chemically sensitive 3D reconstruction. Additionally, low-loss EELS has recently been used to allow a three-dimensional reconstruction of plasmon modes on silver nanocubes [4]. Whilst X-rays and EFTEM mainly allow the mapping of elemental contents, core-loss EELS offers additional possibilities for studying detailed chemistry including bonding and valence states using the near-edge structure. Early studies have already shown the feasibility of core-loss EELS-STEM tomography [5–7]. Nevertheless, EELS signals usually contain a significant amount of multiple scattering, except for the thinnest specimens. This means that the background-subtracted core loss signal is a non-linear function of thickness, which may lead to reconstruction artifacts. The use of single range EELS for 3D reconstruction is therefore only really justifiable for datasets where all projections have a maximum thickness of ~30% of the mean free path for inelastic scattering. Extending EELS tomography to thicker specimens requires explicit account be taken of the multiple scattering, which requires that the low loss and core loss signals are simultaneously acquired, i.e. this necessitates the use of DualEELS [8,9] for the data acquisition. The multiple scattering can be dealt with by using either deconvolution [10] to remove it or modeling [11,12] to take account of it in the quantification. This has recently been used by Habberfehlner et al. [13] to perform chemically sensitive 3D reconstruction of precipitates in an Al–Si alloy containing Yb.

It should be noted that the intensity in an EELS edge is given by the equation:

* Corresponding author at: SUPA School of Physics and Astronomy, University of Glasgow, Glasgow G12 8QQ, UK.

Email address: Ian.MacLaren@glasgow.ac.uk (I. MacLaren)

$I/I_0 = N \sigma$ where I is the intensity for a given energy range above the edge, I_0 is the intensity of the zero loss peak, N is the projected areal density of atoms in the area sampled by the beam and σ is the partial cross-section for the edge of interest for this energy range and for the electron optical parameters used in the experiment (including probe convergence angle, spectrometer collection angle, and primary beam energy). This equation is the basis of all standard EELS quantification routines, although strictly only applies when the spectrum is a single scattering distribution (i.e. no plural scattering) (see Eq. 4.62, p. 270 in [58]). For a constant density material, N will have a linear scaling with thickness and thus, in order to achieve a truly linear relationship between integrated, background-subtracted core-less signals and thickness, the signal I should be normalised by the intensity present in the zero loss peak I_0 . This normalisation is implicit in the model based approach used by Haberfehlner et al. [13] but needs to be performed explicitly if deconvolution, background subtraction and numerical integration of edge intensity is to be used to produce maps for three-dimensional reconstruction.

The present article examines the advantages of using DualEELS for the chemically sensitive reconstruction of vanadium carbide precipitates on an extraction replica prepared from a vanadium microalloyed high manganese steel produced as part of an EU RFCS project (Precipitation in High Manganese Steels). An important step in reconstruction is the alignment procedure. Here a feature-based alignment is used, based on the procedure described in Section S.1 in Supplementary material, following the initial alignment by cross-correlation. A new compressed sensing based algorithm called dictionary learning electron tomography (DLET) [26] is used for the tomographic reconstruction. As it is new, the reliability of the reconstruction is assessed by comparing the experimental reconstruction with a reconstruction from a simulated tomography dataset calculated from a model precipitate in the shape of a perfect octahedron. Experimental data are then reconstructed using both DLET algorithm and the more commonly used simultaneous iterative reconstruction technique (SIRT).

2. Methods

2.1. Materials and sample preparation

As a test object for study, vanadium carbide precipitates from an austenitic high manganese steel are used. The steel composition is 22Mn–0.6C–0.2V–0.01N (wt%–Fe balance) and it was heat treated at 800 °C for 3 h to produce VC_x precipitates a few tens of nm in size. The extraction procedure started with a steel sample with a mirror-polished surface, which was then etched with 2% Nital to reveal the microstructure without damaging the precipitates. Following this, a

30–50 nm carbon film was deposited using an Edwards E306A coating system. Prior to removing the film from the steel, it was scored to provide 3 mm squares. To remove the film with the precipitates attached, the sample was immersed completely in a 20% solution of nitric acid in water. This allowed the detachment of the squared-pieces of carbon replicas. These were then rinsed in ethanol and finally picked up on copper grids for TEM examination.

Vanadium carbide precipitates, with well-developed facets were observed on the replicas. Initial studies have shown that these are often faceted on {111} planes, and that precipitates appearing approximately octahedral in shape are commonly observed. Whilst there have been studies of vanadium carbide or nitride precipitation in steels using advanced analytical scanning transmission electron microscopy (e.g. Epicier et al. [59] and MacKenzie et al. [60]), these are predominantly in ferritic steels where the precipitate-matrix orientation relationship is different and consequently the morphology is different. Recently, a method for the quantitative extraction of the precipitate signal from a steel matrix was published with application to VC in a high Mn steel of similar composition to that studied in this work [61]. The VC precipitate studied in that work seemed to approximate to a cross section consistent with an octahedron.

2.2. Instrumentation and experiment

The tomography experiment was performed on a JEOL ARM200F scanning transmission electron microscope equipped with a cold field emission gun and operated at 200 kV. The probe half-angle was 29 mrad, the probe current was ~400 pA and the probe diameter was ~1 Å.

The acquisition of the datasets and the subsequent processing of tomography data using DualEELS is summarised in Fig. 1. The EELS spectrum image datasets were recorded using a Gatan GIF Quantum ER using a fast DualEELS mode with a drift tube offset of 150 eV between the low loss and high loss datasets. The collection half angle was 36 mrad. The low loss was integrated for 0.000952 s and the high loss for 0.019055 s (i.e. an exposure ratio of 20). The spectrum images were 86 pixels horizontally, but varied in the vertical direction (from 81 to 132 pixels) in order to have sufficient pixels to cover all precipitates of interest (in practice, only a smaller sub-region was used for the reconstruction). Each pixel was 0.99×0.99 nm and the total acquisition time for each DualEELS dataset was about $7\frac{1}{2}$ min.

The sample was held in a JEOL tomography holder which allows a nominal tilt range of $\pm 80^\circ$, although in practice, we were limited to a range of approximately -50° to $+50^\circ$ because of shadowing from grid bars on the sample support. Spectrum images were recorded at 10° intervals in this range starting at $\sim -50^\circ$ and finishing at $\sim +50^\circ$.

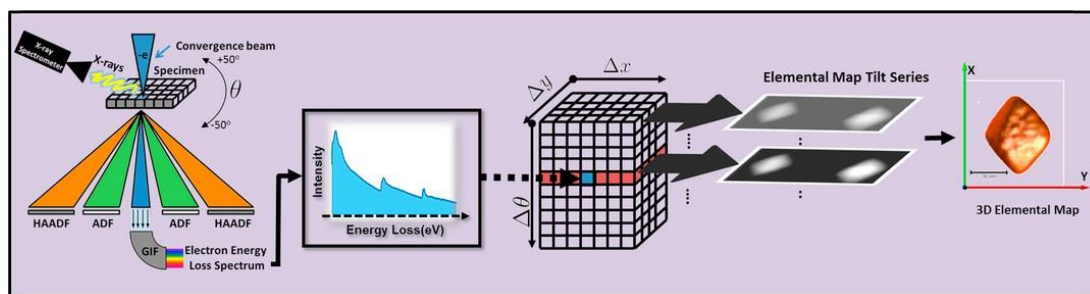


Fig. 1. Schematic illustration of tomography using DualEELS that has been performed in this work – the acquired spectrum-image data set at each tilt in the series is used to generate 2D chemical maps, one for each element under investigation, and thence to reconstruct 3D chemical maps for each element. After [14].

2.3. Post-acquisition procedure

The low loss and high loss spectra were acquired as spectrum images. In a recent publication, a procedure for the extraction of precipitate signals from the two spectrum images was described [15]. The early stages of this procedure were applied in the present case: energy alignment, spectrum cropping, subtraction of any stray signal from the low loss spectrum, noise reduction using principal component analysis [16,17], splicing of the low loss and high loss spectra, and Fourier-log deconvolution to remove the multiple scattering. Following this, vanadium elemental maps were extracted from each spectrum image using background subtraction with a window from 470 to 505 eV and the signals were integrated using a window from 510 to 570 eV. (This energy range is only usable in the absence of any oxygen in the sample, which was the case for this extraction replica). Similarly, for carbon, all maps were produced using a background window from 245 to 275 eV and a signal window from 280 to 340 eV. Finally, all maps were normalised by I_0 , the intensity of the zero loss peak, to produce maps that should have a linear relationship of the intensity to the projected atomic content in each pixel.

Fig. 2 shows HAADF-STEM images and EELS elemental maps of C from the datasets acquired at different tilt angles, together with a spliced and deconvolved EELS spectrum (on a log scale) showing both the low loss and core loss regions in a single spectrum from one pixel on a precipitate in the 0° projection. The tilt axis is vertical in the orientation of this figure. It may be noted that the carbon contri-

tribution from the support is asymmetric about the 0° tilt position and is thicker on the -50° side. This could have occurred either because the carbon replica surface is locally rough, or because it is slightly buckled so that the surface normal is not at 0° . Either way, it seems that the area investigated had a higher angle to the surface normal at -50° than at $+50^\circ$.

The resulting tilt sequences of projected normalised 2D elemental maps for C and V were then aligned to a common tilting axis and used as the input for the tomographic reconstruction as outlined in Fig. 1 (in this case for V).

To allow demonstration of the advantages of using deconvoluted data, a sequence of maps was also created in the same way, but without removing the effects of multiple scattering by deconvolution, but still normalising by division of the edge intensity by I_0 .

To obtain high-quality reconstructed results, accurate alignment is critical before reconstruction. Errors in image registration or alignment to a common tilt axis cause artifacts in the constructed volume [19]. The conventional alignment approach that is commonly used in electron tomography depends on cross-correlation [18,19]. This approach was not accurate in aligning our current dataset. Fig. 3(a) shows an XZ slice from SIRT reconstruction of a tilt series that was aligned using cross-correlation method. The tilt axis still suffers from a degree of misalignment; which causes the reconstruction to smear out into 'arcs'. To overcome this limitation, a feature-based alignment method using contour detection and centre of gravity approach is adopted (see Section S.1 in Supplementary material). The experimental results in Fig. 3(b) indicate that this approach provides accu-

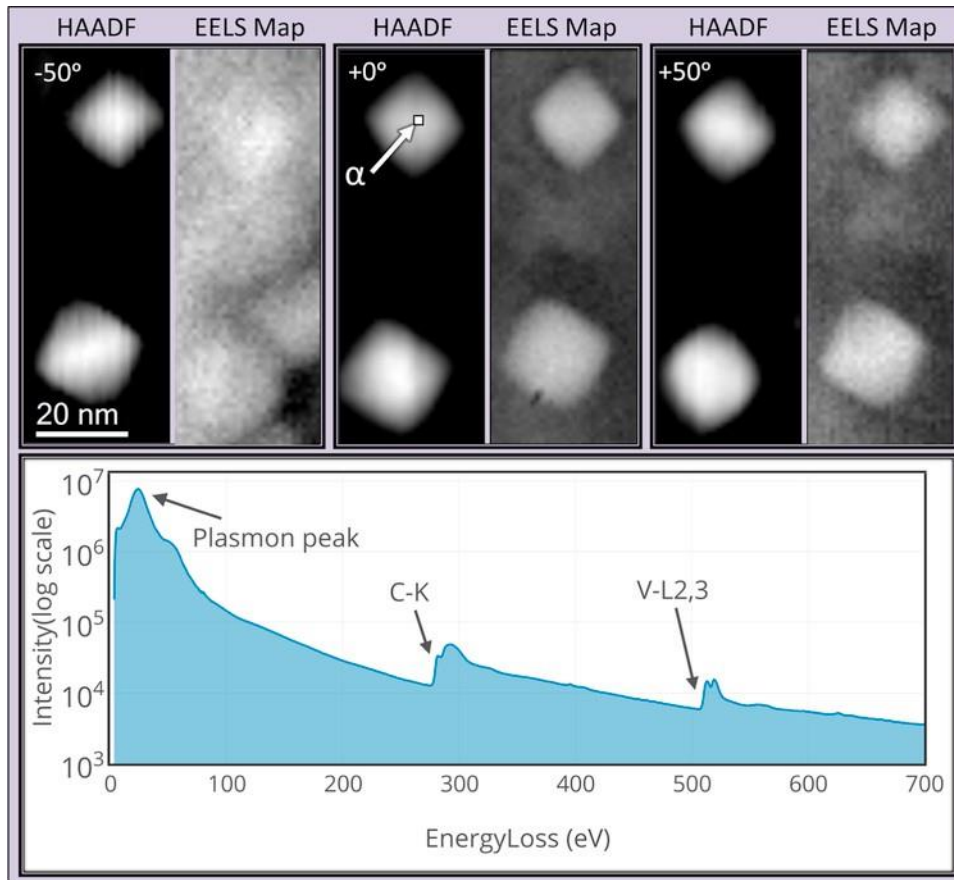


Fig. 2. (Top Row) HAADF-STEM projection 2D image and normalised EELS elemental maps of C from the tilt series. (last Row) A Fourier-ratio deconvolved EELS spectrum extracted from pixel (⊙) in the first precipitate, displayed using a log-linear plot.

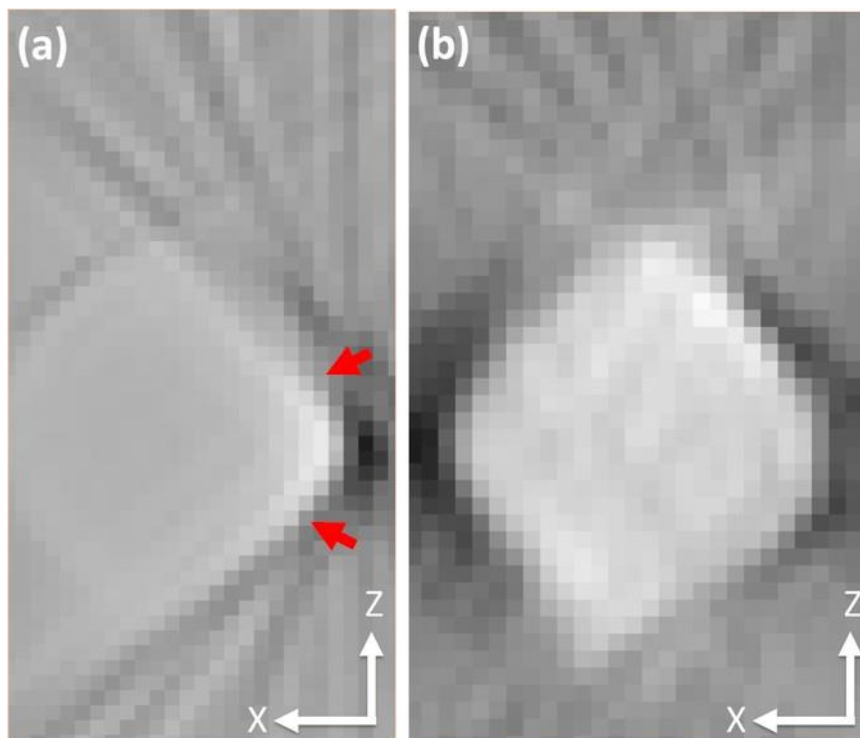


Fig. 3. The effect of tilt-axis misalignment on the reconstruction of a vanadium carbide precipitate. (a) XZ slice from a SIRT Reconstruction of a tilt series that was aligned using a standard cross-correlation method. A distinctive “arcing” artefact is observed, which is a known signature of misalignment. The curvature of this arcing is dependent on the direction and the magnitude of misalignment. (The interested reader is referred to Fig. 11.4 in [24] for further clarification). (b) The same slice after using the improved feature-based alignment procedure described in S.1 in Supplemental material.

rate alignment compared to the cross-correlation method for the dataset in this study.

2.4. Three-dimensional image reconstruction

The reconstruction of 3D elemental maps was performed using both the well-known SIRT algorithm, as well a new compressed sensing based algorithm, DLET [25–27]. SIRT reconstructions were performed using IMOD [21]. Determining the optimal iteration number in SIRT is critical and this is usually selected empirically. Large numbers of iterations will produce a solution that is similar to the weighted back projection algorithm (which can be problematic [26,49]), while very small iterations will produce less accurate reconstruction and lose important features of the tomogram. In this work, the IMOD guideline was followed, which is to select an iteration number in the range 8–25. It was found that 15 iterations provided a visually sensible solution.

The DLET algorithm is based on Compressed Sensing (CS) theory [28,29] and sparse code learning [30]. Compressed sensing has been recently applied to ET [13,31–34] and shows promise for reducing missing wedge artefacts. The use of image sparsity, as a *priori* knowledge to enhance the accuracy of reconstruction, can reduce the number of projections than what is required by conventional techniques. However, most of the applications of CS to ET are based on a fixed sparsifying transform in which, despite its success, the reconstruction quality can be limited. For example, total variation (TV) minimisation can be effective for reconstruction if the object under study can be described as a piecewise constant. However, many samples can be partially sparse under TV transform and this can introduce false structures and artefacts (such as the staircase artefact in Fig. 20(d) in [26]). Other drawbacks of using the TV operator include

over-smoothing of fine structures, difficulties in separating true structures from noise, degradation of spatial resolution (which becomes especially apparent in noisy examples) and sensitivity to reconstruction parameter, which is user-defined and therefore subjective.

DLLET overcomes such limitations by combining the concept of redundancy in CS [35] and sparsity with sparse code learning [30]. This makes it possible to tailor the sparsifying transform in a way that is adapted for specific types of training images. The result enhances the degree of compression and the accuracy of reconstruction. Sparse representation with learned transforms outperforms predefined transforms in a range of image processing applications such as de-noising, de-blurring and in-painting [36–38]. Furthermore, the recent work in Stevens et al. [39] showed the feasibility of using the dictionary learning-based technique to infer missing pixels in STEM images from scanning a random selection of just 5% of the total number of pixels in the image area. In this work, the DLET parallel implementation was run for 20 iterations with the dictionary learning stage performed for 20 iterations. All implementations were executed on Matlab v7.12 (R2013a) installed on a 64-bit Windows 7 operating system with an Intel Core i5 processor running at 3.10 GHz with 24 GB memory and a NVIDIA GPU card with 336 cores.

2.5. Visualisation

Following the image reconstruction step, the constructed volume was then segmented, to generate triangulated surfaces to be visualised. The segmentation was performed using the Otsu method [40], which is an automated thresholding technique to avoid subjective judgment. All visualisation performed here were using AMIRA (FEI – Visualisation Sciences Group). Orthoslices through reconstructions are shown with linear mapping between the maximum and minimum

pixel values in each image. The missing wedge direction is parallel to the z -axis on the orthoslices which is also parallel to the optic axis. The y -axis is parallel to the tilt direction and the x -axis is perpendicular to both. The voxel projection visualisations of the reconstructed volumes were generated using the volume-rendering module in AMIRA with a restricted display windows and the alpha value (overall transparency) decreased until the density from the object(s) prevailed over the background. An arithmetic octahedron was fitted to each surface to provide a visual assessment as in Figs. 5 and 10. The fitting strategy was to find a transform A that applies rotations and a

uniform scale factor that minimises the root mean square distance (Euclidean measure) between the points on the segmented model surface to the corresponding points on the reference octahedron surface. This was performed using the iterative closest point algorithm (ICP) [41].

3. Simulations and experimental results

A simulation study has been performed to support the investigation of the experimental data.

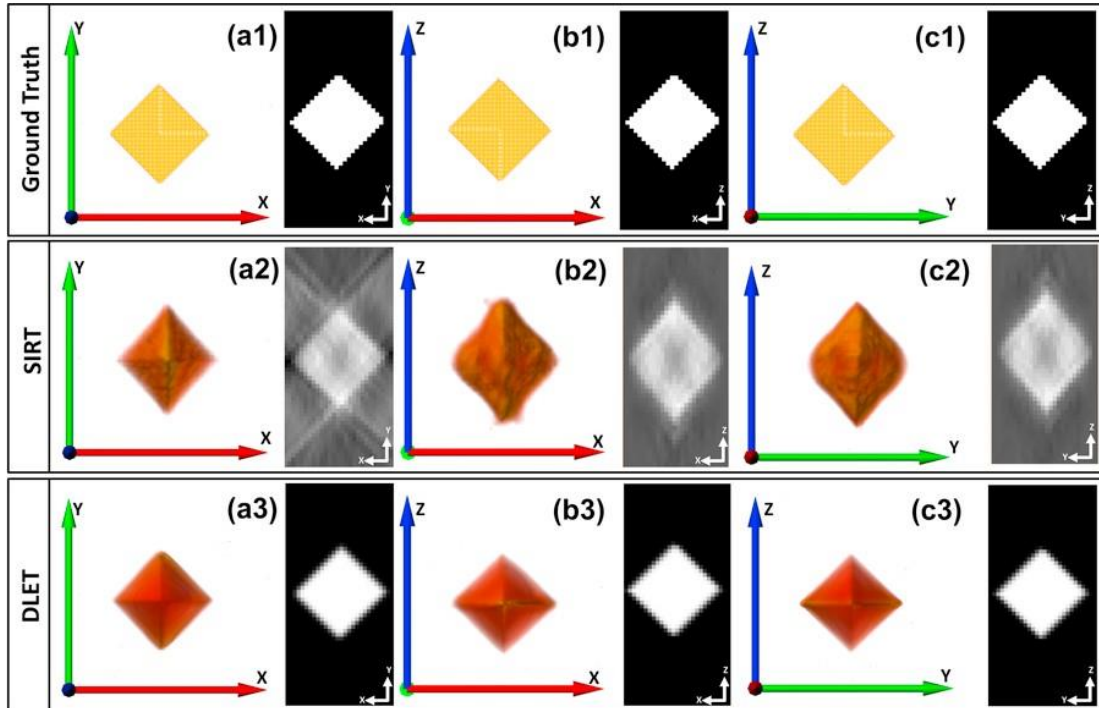


Fig. 4. Simulation of 3D reconstruction of an octahedron from a tilt series of -50° to $+50^\circ$: (a1–c1) volume rendering of the original object along the three principal axes of the octahedron, together with orthoslices taken from the central slice for each the corresponding view (on black backgrounds). (a2–c2) SIRT and (a3–c3) DLET reconstructions from simulated projections, together with their central orthoslices. For visualisation purposes, the image intensities of the orthoslices were enhanced.

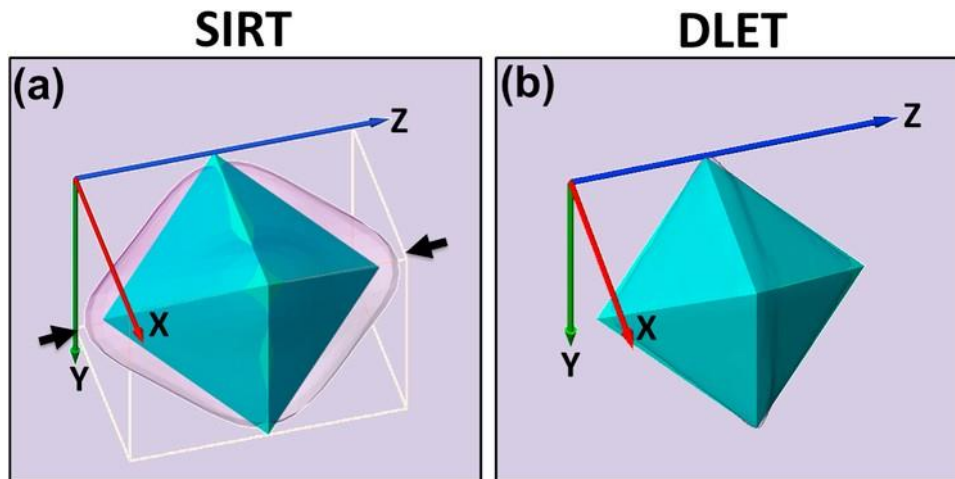


Fig. 5. A comparison of reconstructions of the simulated octahedron VC_x using (a) SIRT and the (b) DLET algorithm showing a comparison to an idealised octahedron. Note that the distortion in the z (missing wedge) direction is much reduced using DLET.

3.1. Simulation study: reconstructions on simulated tilt series from an idealised octahedron

Since the precipitates are expected to approximate to octahedra in shape, a regular octahedral precipitate was computer generated and the imaging process was then simulated upon these precipitates. The simulated tilt series were obtained taking into consideration the imaging conditions, such as detector resolution, bit depth and intensity. ET reconstruction was then performed on the simulated tilt series.

3.1.1. Generation of simulated octahedral precipitate tilt series

The simulated test object should have one solid component shaped as a regular octahedron, defined as the shape which is formed by connecting all the face centres of a cube. This will have 8 faces, angles between edges are 90° , and angles between faces meeting at an edge are 70.5° and angles between sides meeting across a point are 109.5° . To simulate the experimental data as closely as possible, a 3D model (mesh model) was created using CAD software. This mesh model was then voxelised using the method of Patil and Ravi [42]. The voxelisation involves converting objects from continuous geometric form into voxels representation that best approximates the original object. The result is a binary 3D matrix with voxel values of logical 1 to represent the boundary and inside region of a 3D object of constant density or 0 to represent the background. This 3D matrix was spatially quantised in a way that simulates the ideal output from the detector of the STEM imaging process (i.e. each octahedron object requires a box of approximately 23^3 pixels to be represented in a similar way to the real precipitates in the experimental EELS elemental-map tilt series). Fig. 4(a1–c1) shows the simulated octahedron from three orthogonal projections. To simulate the imaging process, the Radon transform for parallel-beam geometry was performed upon the sampled 3D matrix at 10° intervals from $\pm 50^\circ$ rotations. Then, shot and quantisation noise were added to the simulated images. All simulation generation was performed using MATLAB (Mathworks Inc.), reconstructed using IMOD [21] and visualised using AMIRA (FEI). The Radon transform represents the path-length of the rays in the material, which was determined by taking line integrals through the sample between the source and detector to generate the projection image I_{out} . The simulated projections were scaled to have a mean value equal to the mean of the EELS elemental maps, and subsequently corrupted by shot, Gaussian and quantisation noise to obtain a low SNR dataset. This should nicely approximate the signal seen by HAADF imaging in the STEM (which should be close to linear for low object thicknesses) or EELS edge intensities, after correction for multiple scattering and normalisation by I_0 (which should be completely linear with thickness).

3.1.2. Addition of noise and quantisation

It was assumed that only shot and Gaussian noise are present in the detected intensity. The shot noise arises because the electrons arrive at the detector at random. Due to this, the number of the detected electrons in a time interval will vary, following Poisson statistics. The signal to noise ratio of the value on each pixel is equal to. A noisy Gaussian background of standard deviation ρ was added to the projections, to simulate electronic noise in the amplifier system, resulting in a dataset with reduced SNR. The ρ parameter was approximated to mimic the experimental projections.

In any electron detecting system, there are a limited number of possible discrete values of electrons that can be detected. For digital processing, the continuous intensity of detected intensity needs to be converted into a discrete value, (i.e. quantised). Quantisation is the

process by which a value on a continuous scale of measurement is mapped to a discrete value. Quantising with L bit depth gives discrete intensity values that can be assigned. The mapping between quantised and detected intensity was assumed to be equal I_{out} . The formula for the quantised intensity I_Q at each pixel after the addition of noise is:

$$I_Q = \lfloor 2^L \frac{P(I_{out}) + N(I_{out}, \rho)}{I_{in}} \rfloor \quad (1)$$

Where $P(x)$ returns a random value from Poisson distribution (with a mean and variance of x) and L is the pixel bit depth and $N(x)$ returns a random value from a Gaussian distribution with a mean of x and variance of ρ .

With the phantom images as the ground truth, the reconstructed simulation was assessed in terms of two commonly used metrics: Peak Signal-to-Noise Ratio (PSNR) [43] and Structural SIMilarity (SSIM) index [44]. PSNR was obtained as ratio between the signal's maximum powers (peak reference intensity) to the power of the signal's noise (root mean square of reconstruction error). The PSNR is measured in decibels (dB) and the higher the PSNR value, the better the quality of the reconstruction. Although the PSNR is a simple mathematical metric that is commonly used as a distortion metric, it usually does not correlate closely with perceived image quality [45]. This is why we have chosen to use a different, and more advanced metric, the SSIM. The SSIM index range between 0–100% and has been shown to be consistent with visual perception as can be seen in [44].

3.1.3. Simulation results

Fig. 4(a2–c3) shows the SIRT and DLET reconstructions from the simulated 10 projection tilt-series of a vanadium carbide octahedron. As can be seen, the SIRT reconstruction clearly suffers from elongation and boundaries blurring in the missing wedge (z) direction. Also, as expected, it suffers from streaking artefacts due to the limited angular range. These artefacts are obviously reduced in the corresponding DLET reconstruction as can be seen in Fig. 4 (a3–c3), where it is clear that the DLET reconstruction has accurately recovered the simulated 3D phantom. Also, the denoising capability of the adaptive sparsifying transform in DLET has produced a near uniform intensity across the background. It should further be noted that SIRT orthoslices falsely show a reduced density in the voxels in the centre of the octahedron, whereas the correct uniform density through the octahedron is reproduced by reconstruction with the DLET algorithm. The quality metrics for the reconstruction (Table 1) confirm the effectiveness of the adaptive sparsifying transform.

Fig. 5 shows the result of fitting the reconstruction results from simulations to an idealised octahedron. The SIRT reconstruction (as indicated by the arrows in Fig. 5a) is elongated in the missing wedge (z -direction). This artefact is significantly reduced in the DLET reconstruction as shown in (Fig. 5b), suggesting that DLET will be much more effective in working with this kind of data with a significant missing wedge and relatively coarse angular steps.

Table 1
Quality metric values of simulation reconstruction in Fig. 4.

Method/metric	PSNR	SSIM
SIRT	16.61	29.25%
DLLET	19.51	82.26%

3.2. Experimental study: reconstructions on experimental maps from DualEELS

After creating 11 different maps from the DualEELS spectrum images of an area containing two precipitates, the 3D vanadium distribution was reconstructed using both SIRT and DLET. The resulting reconstruction comparison is shown in Fig. 6. Orthoslices through reconstructed EELS elemental maps of the VC_x precipitate from the V-L_{2,3} signal are shown to the top in a1-aiii for SIRT and to the bottom in b1-biii for DLET. As can be seen, DLET provided a reconstruction with reduced noise and a clear separation between the precipitates and the background signal. This makes the segmentation step much more straightforward and provides high-fidelity surfaces for quantitative analysis. For comparison, a 3D reconstruction performed on the HAADF signal recorded simultaneously with the collection of the DualEELS spectrum images is shown in Fig. 7. (a1–a3) are for SIRT and (a2–a3) are for DLET. The HAADF data reconstructs in a very similar manner to the EELS, giving confidence that the reconstruction is reliable.

It is also clear that the use of DLET together with DualEELS to accurately reconstruct a signal that is a linear function of thickness has resulted in well-behaved orthoslices with constant density throughout the thickness (i.e. no cupping artefacts [46,47]), as is clearly shown in the line profiles in Fig. 8(c) and (d) for both the V-L_{2,3} maps and the HAADF maps.

SIRT reconstructions in Fig. 8(a) and (b) also show absence of cupping artefacts, however, the line profiles are clearly more curved and it is difficult to segment the precipitate's boundaries accurately. The SIRT reconstruction also shows a high background noise level. The DLET reconstruction shows a near steady intensity across the background. Additionally, the SIRT reconstruction of the precipitate is of lower contrast and lower intensity, compared to the DLET reconstruction. This is probably due to a well-known limitation of SIRT, where the intensity of the reconstructed precipitates can be influenced by their size [50].

For comparison, a DLET reconstruction is also shown using EELS maps made without deconvolution to remove the effects of plural scattering in the spectra (Fig. 8-e) together with the same profile through the centre of the precipitate (Fig. 8-f). In this case, even in a relatively thin precipitate, there is a subtle, but noticeable cupping artefact. It is anticipated that such artefacts would be far worse in thicker precipitates examined with EELS tomography.

The streaking and blurring present after using SIRT is also absent in the DLET reconstruction. These results accord well with the simulation study, and it is clear that reconstruction using DLET has massively outperformed SIRT for reconstruction fidelity, and the results are particularly impressive considering just 11 projections were used. This really demonstrates the usefulness of this compressed sensing approach to 3D reconstruction of spectroscopic mapping data – such data is always likely to be limited in signal to noise by its very nature, since the total possible signal will be limited by either how much radiation dose can be applied to the sample before it is altered significantly or by the available time for data collection.

For a further comparison of SIRT versus DLET, Fig. 9 shows surface rendered views of segmented 3D EELS elemental map fitted to idealised octahedra, again showing very clearly the massive z-elongation that results from the use of SIRT, just as was predicted in our simulation study above. ESI Video S1 in the supplemental information shows 360° volume rendering views and the segmented surface of the reconstructed EELS dataset. It should be noted, that whilst the precipitate approximates to an ideal octahedron, corners and edges are not as sharp as in the ideal geometric shape: this is entirely as would be expected since single atoms for corners or lines of single atoms for edges are unlikely to be thermodynamically stable, and it is likely that both corners and edges would be somewhat rounded to minimise surface energy.

Supplementary material related to this article can be found online at doi:10.1016/j.ultramic.2016.08.004.

With the benefit of the DLET algorithm in combination with EELS maps for C and V from deconvoluted data, it is therefore possible to produce 3D renderings of the actual structure of the carbon ex-

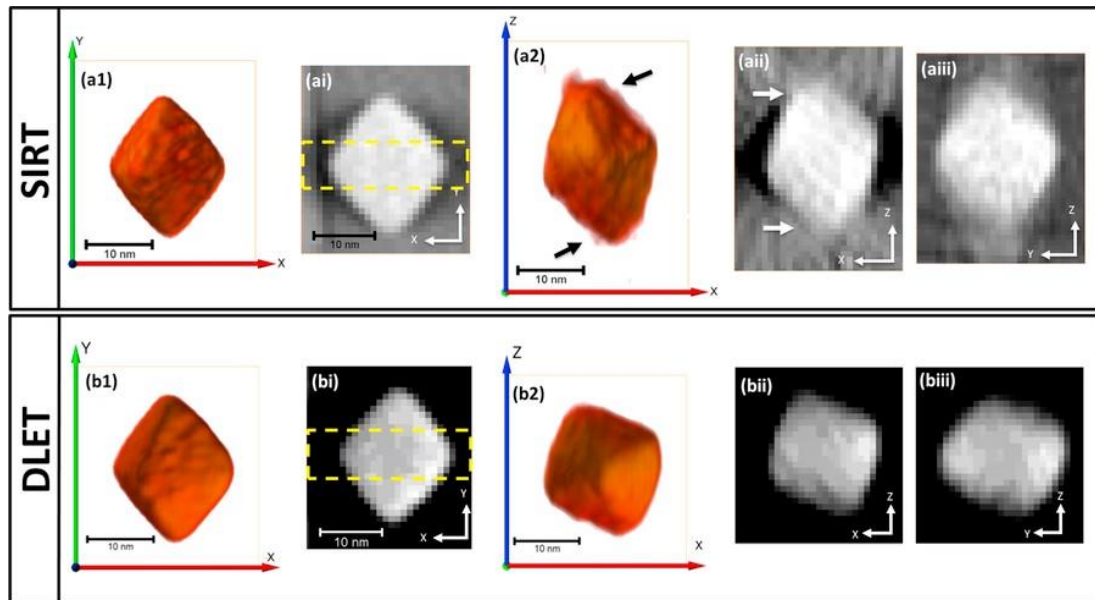


Fig. 6. Reconstructions of the Vanadium signal in VC precipitates from the experimental DualEELS tomography tilt-series. (a1–a2) 3D perspective view of reconstructions using SIRT. (ai–aiii) Orthogonal slices through the SIRT reconstruction were extracted respectively from (a1–a2). (b1–b2) 3D perspective view from which (bi–biii) were extracted, respectively.

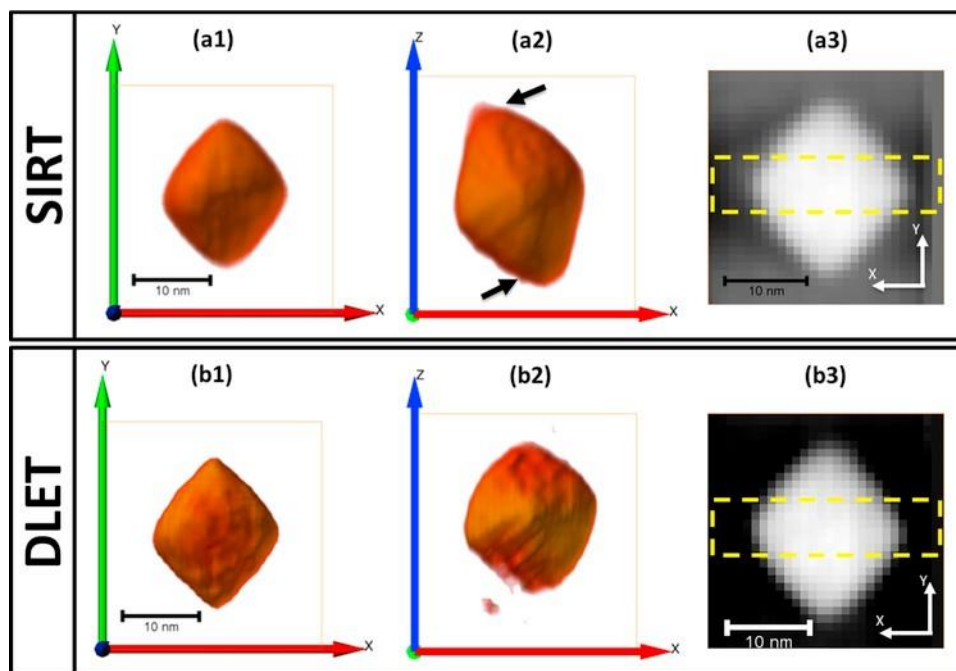


Fig. 7. Reconstructions of Vanadium precipitates from the experimental HAADF signal recorded simultaneously with EELS dataset. (a1–a2) 3D perspective view voxel projections of reconstruction using SIRT, (a3) Orthogonal slice through the centre of volume in a1. (b2–b2) 3D perspective view voxel projections of reconstruction using DLET, (b3) Orthogonal slice through the centre of volume in b1.

traction replica, as shown in Fig. 10, showing both the carbon and the partially embedded VC precipitates. A full 3D rendering of this is also shown in ESI Video S2 in the supplemental material. Perhaps unsurprisingly, parts of the precipitates are encapsulated within the carbon, whilst other parts protrude beyond it. Moreover, the roughness of the carbon surface is clear, which is a reflection of the surface roughness of the steel that the replica was extracted from after the initial etch. The use of such 3D reconstructions may in future also help to better understand the replica extraction process.

Supplementary material related to this article can be found online at doi:10.1016/j.ultramic.2016.08.004.

4. Conclusion

It is shown in this paper that using DualEELS to generate EELS maps without multiple scattering through Fourier-log deconvolution and normalisation by the zero loss peak intensity is important for the correct 3D reconstruction of the chemistry of materials using EELS tomography, since only after deconvolution and normalisation is there a truly linear relationship between edge intensity and thickness. It is shown that not performing deconvolution can lead to cupping artefacts (i.e. centres of apparently lower density than the edges), whereas once deconvolution has been applied, these artefacts are absent. This use of deconvoluted EELS data for map generation when combined with a new compressed sensing algorithm (Dictionary Learning Electron Tomography – DLET), is shown in both simulation and experiment to do an excellent job of reconstructing the 3D

shape of octahedral vanadium carbide precipitates. These are shown to deviate slightly from pure octahedra in reality, as would be expected due to the thermodynamic instability of sharp edges and corners, but the use of the DLET algorithm was key to understanding this properly without distortions, since the older SIRT algorithm distorts the shape significantly in the missing wedge (z) direction. This then allows the correct 3D chemically-sensitive representation of complex inhomogeneous nanostructures, such as the carbon extraction replicas of vanadium carbide studied in this work.

Uncited references

Acknowledgment

AAA acknowledges funding for a Ph.D. studentship from the Lord Kelvin/Adam Smith Scholarship of the University of Glasgow. The work on high-Mn steels was funded by the EU Research Fund for Coal and Steel (Precipitation in High Manganese Steels, RFSR-CT-2010-00018). This work was made possible by generous provision of the MagTEM facility by SUPA and the University of Glasgow.

Appendix A. Supplementary material

Supplementary data associated with this article can be found in the online version at doi:10.1016/j.ultramic.2016.08.004.

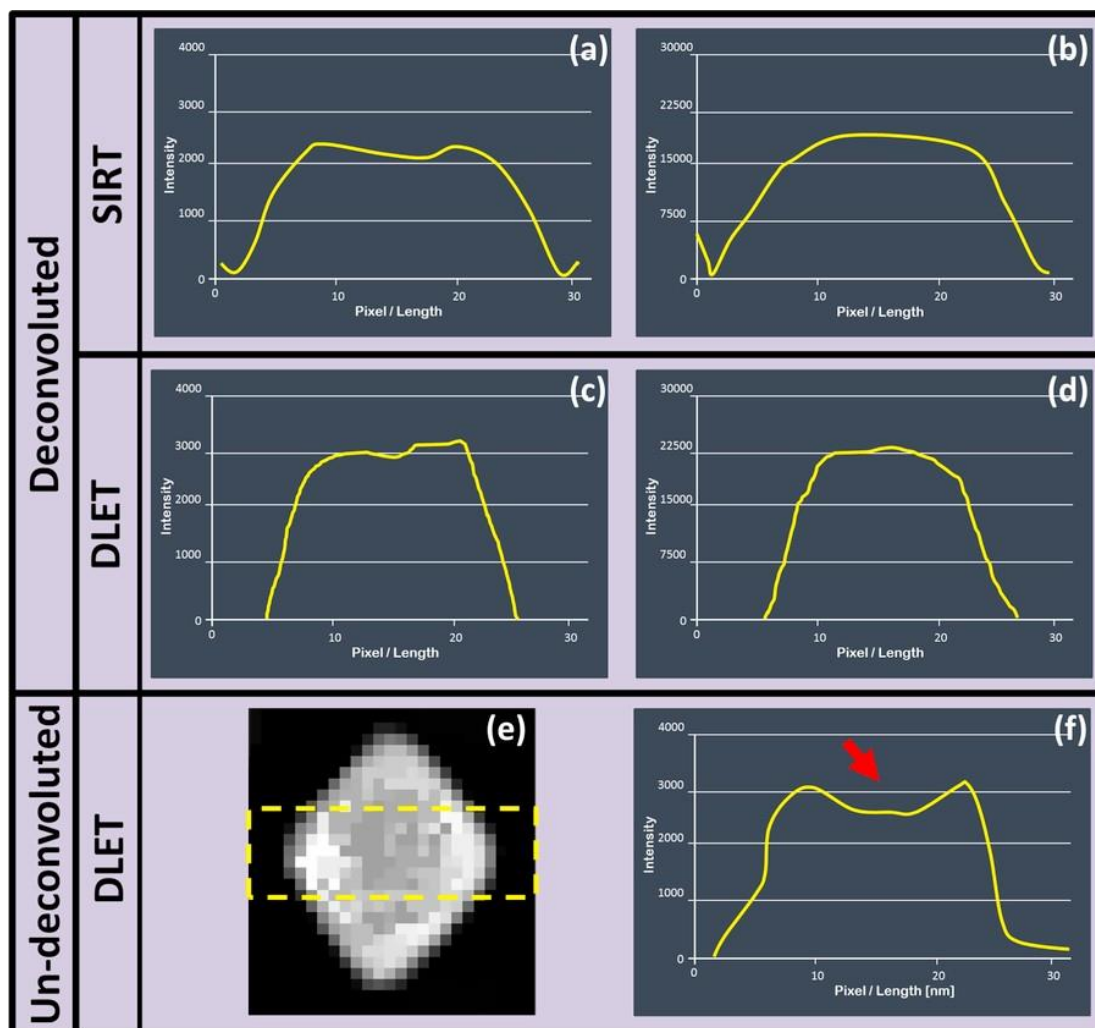


Fig. 8. Average line profile through the region of the orthoslices between the yellow dotted lines indicated in (a) Fig. 6-ai, which is a SIRT reconstruction of EELS elemental maps (b) Fig. 7-a3, which is a SIRT reconstruction of HAADF tilt series. (c) Fig. 6-bi, which is a DLET reconstruction of EELS elemental maps, and (d) Fig. 7-b3, which is a DLET reconstruction of HAADF tilt series. Neither shows any cupping artefacts. Cupping artefacts resulting from omitting deconvolution to remove multiple scattering from the EELS data. (e) Orthogonal slice through the centre of the DLET 3D reconstruction from the raw normalised $V-L_{2,3}$ signal (i.e. without applying deconvolution), (f) Average Line profile integrated vertically through the dotted area indicated in (e).

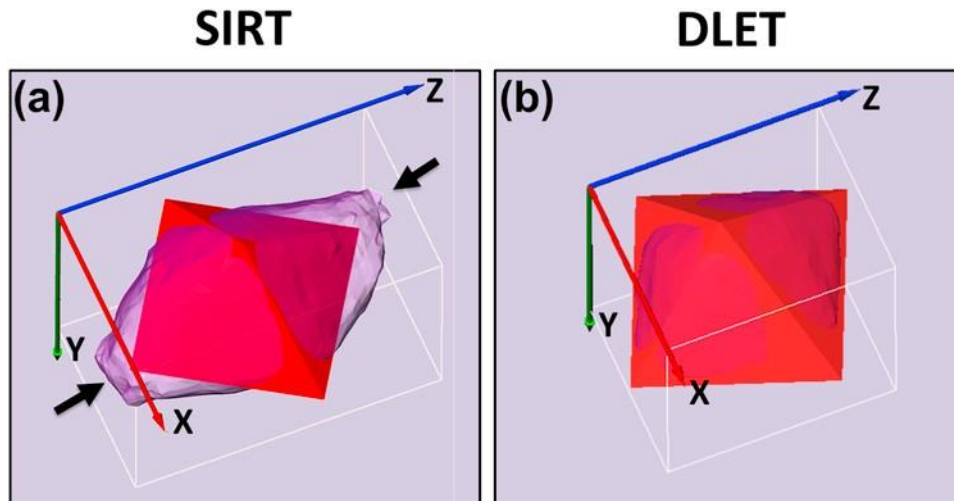


Fig. 9. A comparison of reconstructions of the VC precipitate from the V-L2 signal using (a) SIRT and the (b) DLET algorithm showing a comparison to an idealised octahedron. Note that the distortion in the Z (missing wedge) direction is much reduced using DLET.

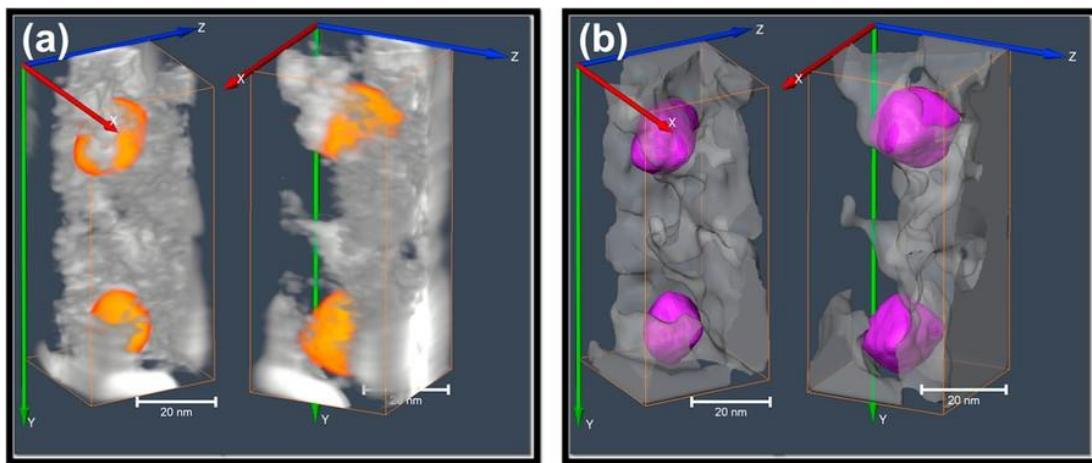


Fig. 10. (a) Volume rendered views of the combined volume resulted from reconstructions of Vanadium Maps and Carbon maps. (b) Surface rendered views of the segmented volume of (a).

References

- [1] W. Baumeister, Electron tomography of molecules and cells, *Trends Cell Biol.* 9 (2) (1999) 81–85.
- [2] P.A. Midgley, E.P.W. Ward, A.B. Hungria, J.M. Thomas, Nanotomography in the chemical biological and materials sciences, *Chem. Soc. Rev.* 36 (9) (2007) 1477.
- [3] P.W. Hawkes, The electron microscope as a structure projector, in: Joachim Frank (Ed.), *Electron Tomography*, Springer Science Business Media, 2006, pp. 83–111.
- [4] O. Nicoletti, F. de la Peña, R.K. Leary, D.J. Holland, C. Ducati, P.A. Midgley, Three-dimensional imaging of localized surface plasmon resonances of metal nanoparticles, *Nature* 502 (7469) (2013) 80–84.
- [5] K. Jarausch, P. Thomas, D.N. Leonard, R. Twesten, C.R. Booth, Four-dimensional STEM-EELS: Enabling nano-scale chemical tomography, *Ultramicroscopy* 109 (4) (2009) 326–337.
- [6] L. Yedra, A. Eljarrat, R. Arenal, E. Pellicer, M. Cabo, A. López-Ortega, M. Estrader, J. Sort, M.D. Baró, S. Estradé, F. Peiró, EEL spectroscopic tomography: towards a new dimension in nanomaterials analysis, *Ultramicroscopy* 122 (2012) 12–18.
- [7] L. Yedra, A. Eljarrat, J.M. Rebled, L. López-Conesa, N. Dix, F. Sánchez, S. Estradé, F. Peiró, EELS tomography in multiferroic nanocomposites: from spectrum images to the spectrum volume, *Nanoscale* 6 (12) (2014) 6646.
- [8] J. Scott, P. Thomas, M. MacKenzie, S. McFadzean, J. Wilbrink, A. Craven, W. Nicholson, Near-simultaneous dual energy range EELS spectrum imaging, *Ultramicroscopy* 108 (12) (2008) 1586–1594.
- [9] A. Gubbens, M. Barfels, C. Trevor, R. Twesten, P. Mooney, P. Thomas, N. Menon, B. Kraus, C. Mao, B. McGinn, The GIF quantum a next generation post-column imaging energy filter, *Ultramicroscopy* 110 (8) (2010) 962–970.
- [10] R.F. Egerton, Electron energy-loss spectroscopy in the TEM, *Rep. Prog. Phys.* 72 (1) (2008) 016502.
- [11] J. Verbeeck, S.V. Aert, Model based quantification of EELS spectra, *Ultramicroscopy* 101 (2–4) (2004) 207–224.
- [12] P. Thomas, R. Twesten, A simple model based approach for robust quantification of EELS spectra and spectrum-images, *Microsc. Microanal.* 18 (S2) (2012) 968–969.
- [13] G. Haberfehlner, A. Orthacker, M. Albu, J. Li, G. Kothleitner, Nanoscale voxel spectroscopy by simultaneous EELS and EDS tomography, *Nanoscale* 6 (23) (2014) 14563–14569.
- [14] A. Maigné, R. Twesten, Review of recent advances in spectrum imaging and its extension to reciprocal space, *J. Electron Microsc.* 58 (2009) 99–109.
- [15] J. Bobynko, I. MacLaren, A.J. Craven, Spectrum imaging of complex nanostructures using DualEELS: I. digital extraction replicas, *Ultramicroscopy* 149 (2015) 9–20.
- [16] M. Bosman, M. Watanabe, D. Alexander, V. Keast, Mapping chemical and bonding information using multivariate analysis of electron energy-loss spectrum images, *Ultramicroscopy* 106 (11–12) (2006) 1024–1032.

- [17] G. Lucas, P. Burdet, M. Cantoni, C. Hébert, Multivariate statistical analysis as a tool for the segmentation of 3D spectral data, *Micron* 52–53 (2013) 49–56.
- [18] R. Guckenberger, Determination of a common origin in the micrographs of tilt series in three-dimensional electron microscopy, *Ultramicroscopy* 9 (1–2) (1982) 167–173.
- [19] J. Frank (Ed.), *Electron Tomography*, Springer, New York, 2006.
- [20] .
- [21] D. Mastrorade, Tomographic reconstruction with the IMOD software package, *Microsc. Microanal.* 12 (S02) (2006) 178–179.
- [22] J. Banhart, *Advanced Tomographic Methods in Materials Research and Engineering*, Oxford University Press, New York, 2008.
- [23] A. AlAfeef, P. Cockshott, I. MacLaren, S. McVitie, Compressed sensing electron tomography using adaptive dictionaries: a simulation study, *J. Phys.: Conf. Ser.* 522 (2014) 012021.
- [24] A. Al-Afeef, W.P. Cockshott, I. MacLaren, S. McVitie, Electron tomography image reconstruction using data-driven adaptive compressed sensing, *Scanning* (2015) <http://dx.doi.org/10.1002/sca.21271> (early view).
- [25] A. AlAfeef, W. Cockshott, I. MacLaren, Dictionary based reconstruction of the 3D morphology of Ebola virus, in: *Microscopy and Microanalysis MM2015*, 2015, paper: 1172
- [26] D. Donoho, Compressed sensing, *IEEE Trans. Inf. Theory* 52 (4) (2006) 1289–1306.
- [27] E. Candes, J. Romberg, T. Tao, Robust uncertainty principles: exact signal reconstruction from highly incomplete frequency information, *IEEE Trans. Inf. Theory* 52 (2) (2006) 489–509.
- [28] B.A. Olshausen, D.J. Field, Emergence of simple-cell receptive field properties by learning a sparse code for natural images, *Nature* 381 (6583) (1996) 607–609.
- [29] Z. Saghi, D.J. Holland, R. Leary, A. Falqui, G. Bertoni, A.J. Sederman, L.F. Gladden, P.A. Midgley, Three-dimensional morphology of iron oxide nanoparticles with reactive concave surfaces. A compressed sensing–electron tomography (CS-ET) approach, *Nano Lett.* 11 (11) (2011) 4666–4673.
- [30] B. Goris, W.V. den Broek, K. Batenburg, H.H. Mezerji, S. Bals, Electron tomography based on a total variation minimization reconstruction technique, *Ultramicroscopy* 113 (2012) 120–130.
- [31] N. Monsegue, X. Jin, T. Echigo, G. Wang, M. Murayama, Three-dimensional characterization of iron oxide ($\text{-Fe}_2\text{O}_3$) nanoparticles: application of a compressed sensing inspired reconstruction algorithm to electron tomography, *Microsc. Microanal.* 18 (06) (2012) 1362–1367.
- [32] R. Leary, Z. Saghi, P.A. Midgley, D.J. Holland, Compressed sensing electron tomography, *Ultramicroscopy* 131 (2013) 70–91.
- [33] H. Rauhut, K. Schnass, P. Vandergheynst, Compressed sensing and redundant dictionaries, *IEEE Trans. Inf. Theory* 54 (5) (2008) 2210–2219.
- [34] M. Aharon, M. Elad, A.M. Bruckstein, On the uniqueness of overcomplete dictionaries and a practical way to retrieve them, *Linear Algebra Appl.* 416 (1) (2006) 48–67.
- [35] H. Li, F. Liu, Image Denoising Via Sparse and Redundant Representations Over Learned Dictionaries in Wavelet Domain, in: *Proceedings of the 2009 Fifth International Conference on Image and Graphics*, IEEE, 2009.
- [36] J. Mairal, M. Elad, G. Sapiro, Sparse representation for color image restoration, *IEEE Trans. Image Process.* 17 (1) (2008) 53–69.
- [37] A. Stevens, H. Yang, L. Carin, I. Arslan, N.D. Browning, The potential for Bayesian compressive sensing to significantly reduce electron dose in high-resolution STEM images, *Microscopy* 63 (1) (2013) 41–51, <http://dx.doi.org/10.1093/jmicro/dfi042>.
- [38] N. Otsu, A threshold selection method from gray-level histograms, *Automatica* 11 (285–296) (1975) 23–27.
- [39] P. Besl, H. McKay, A method for registration of 3-D shapes, *IEEE Trans. Pattern Anal. Mach. Intell.* 14 (2) (1992) 239–256.
- [40] S. Patil, B. Ravi, Voxel-based representation display and thickness analysis of intricate shapes, in: *Proceedings of the Ninth International Conference on Computer Aided Design and Computer Graphics (CAD-CG05)*, IEEE, 2005.
- [41] Q. Huynh-Thu, M. Ghanbari, Scope of validity of PSNR in image/video quality assessment, *Electron. Lett.* 44 (13) (2008) 800.
- [42] Z. Wang, A. Bovik, H. Sheikh, E. Simoncelli, Image quality assessment: from error visibility to structural similarity, *IEEE Trans. Image Process.* 13 (4) (2004) 600–612.
- [43] D. Chandler, S. Hemami, VSNR: a wavelet-based visual signal-to-noise ratio for natural images, *IEEE Trans. Image Process.* 16 (9) (2007) 2284–2298.
- [44] Z. Saghi, X. Xu, G. Möbus, Electron tomography of regularly shaped nanostructures under non-linear image acquisition, *J. Microsc.* 232 (2008) 186–195.
- [45] W. Van den Broek, A. Rosenauer, B. Goris, G. Martinez, S. Bals, S. Van Aert, D. Van Dyck, Correction of non-linear thickness effects in HAADF STEM electron tomography, *Ultramicroscopy* 116 (2012) 8–12.
- [46] P.C. Hansen, *Discrete Inverse Problems: Insight and Algorithms*, vol. 7, Siam., 2010.
- [47] C. Kuebel, M. Godehardt, R. Cieslinski, S. Rozeveld, Towards a quantitative understanding in electron tomography, *Microsc. Microanal.* 15 (2) (2009) 602–603.
- [48] Z. Saghi, X. Xu, Y. Peng, B. Inkson, G. Möbus, Three-dimensional chemical analysis of tungsten probes by energy dispersive x-ray nanotomography, *Appl. Phys. Lett.* 91 (25) (2007) 251906.
- [49] A. Genc, L. Kovarik, M. Gu, H. Cheng, P. Pullan Plachinda, C., L. Wang, XEDS STEM tomography for 3D chemical characterization of nanoscale particles, *Ultramicroscopy* 131 (2013) 24–32.
- [50] G. Möbus, R.C. Doole, B.J. Inkson, Spectroscopic electron tomography, *Ultramicroscopy* 96 (3) (2003) 433–451.
- [51] G. Möbus, B.J. Inkson, Three-dimensional reconstruction of buried nanoparticles by element-sensitive tomography based on in elastically scattered electrons, *Appl. Phys. Lett.* 79 (9) (2001) 1369–1371.
- [52] G. Haberfehlner, P. Bayle-Guillemaud, G. Audoit, D. Lafond, P.H. Morel, V. Jousseau, P. Bleu, Four-dimensional spectral low-loss energy-filtered transmission electron tomography of silicon nanowire-based capacitors, *Appl. Phys. Lett.* 101 (6) (2012) 063108.
- [53] M. Weyland, P.A. Midgley, Extending energy-filtered transmission electron microscopy (EFTEM) into three dimensions using electron tomography, *Microsc. Microanal.* 9 (06) (2003) 542–555.
- [54] K. Jarausch, P. Thomas, D.N. Leonard, R. Twisten, C.R. Booth, Four-dimensional STEM-EELS: enabling nano-scale chemical tomography, *Ultramicroscopy* 109 (4) (2009) 326–337.
- [55] R.F. Egerton, *Electron Energy-Loss Spectroscopy in the Electron Microscope*, 3rd ed., Springer Science & Business Media, 2011.
- [56] T. Epicier, D. Acevedo, M. Perez, Crystallographic structure of vanadium carbide precipitates in a model Fe–C–V steel, *Philos. Mag.* 88 (1) (2008) 31–45.
- [57] M. MacKenzie, A.J. Craven, C.L. Collins, Nanoanalysis of very fine VN precipitates in steel, *Scr. Mater.* 54 (1) (2006) 1–5.
- [58] J. Bobynko, I. MacLaren, L., A.J. Craven, Spectrum imaging of complex nanostructures using DualEELS: I. digital extraction replicas, *Ultramicroscopy* 149 (2015) (2015) 9–20.